

NONLINEAR AND LINEARIZED GRAY BOX MODELS OF DIRECT-WRITE PRINTING DYNAMICS

A. Simeunovic*, D. Hoelzle*

*Department of Mechanical and Aerospace Engineering, The Ohio State University,
Columbus, OH 43210

Abstract

Control of material metering in material extrusion based additive manufacturing modalities, such as positive displacement direct-write, is critical for manufacturing accuracy. However, in positive displacement direct-write, transient flows are poorly controlled due to capacitive pressure dynamics - pressure is stored and slowly released over time from the build material and other compliant system elements, negatively impacting flow rate start-ups and stops. Thus far, modeling of these dynamics has ranged from simplistic, potentially omitting key contributors to the observed phenomena, to highly complex, making usage in control schemes difficult. Here, we present nonlinear and linearized models that seek to both capture the capacitive and nonlinear resistive fluid elements of positive displacement direct-write systems and to pose them as ordinary differential equations for integration into nonlinear and linear control schemes. We validate our theoretical work with experimental flow rate and material measurements across a range of extrusion nozzles and materials to address different feature sizes and diverse applications spanning tissue engineering, electronics fabrication, and food science. As part of this experimental work, we explore the contribution of the bulk system compliance and the build material compliance to these dynamics. We show that all models accurately describe the measured dynamics, facilitating ease of integration into future nonlinear and linear control systems. Additionally, we show that while build material compliance may be nearly entirely reduced through appropriate system design, the compliance from build material alone is significant enough to require feedback control to fully control material delivery.

1 Introduction

Currently, additive manufacturing (AM) is widespread in many industries [1], with varying AM modalities used to fabricate constructs as diverse as polymers, metals [2], glass [3], and synthetic tissues [4][5]. Of these modalities, direct-write (DW) printing has gained popularity for its simplicity, ability to directly deliver material, ability to create multi-material domains, and material diversity. DW printing (also termed microextrusion, robocasting, or micro-robotic deposition) is an AM method whereby the build material is extruded through a nozzle by a mechanical plunger or pressurized air as the nozzle moves in three-dimensional space across a printing platform [6] (Fig. 1a, 1b). However, this leads to the fundamental mechanism of action of DW resulting in capacitive pressure dynamics,

which lead to poor deposition control in transient flows. For example, consider the fabrication of simple, two-dimensional shapes utilizing hydroxyapatite, a DW build material that has been used in printing of synthetic tissue scaffolds (Fig. 1c). In both circle and triangle constructs, flow takes time to develop as printing begins and time to end once input flow rate has stopped. This leads to a lack of material at the start of constructs and undesirable material at the end. Even with a small volume of material delivered, lack of flow control during starts and stops is evident.

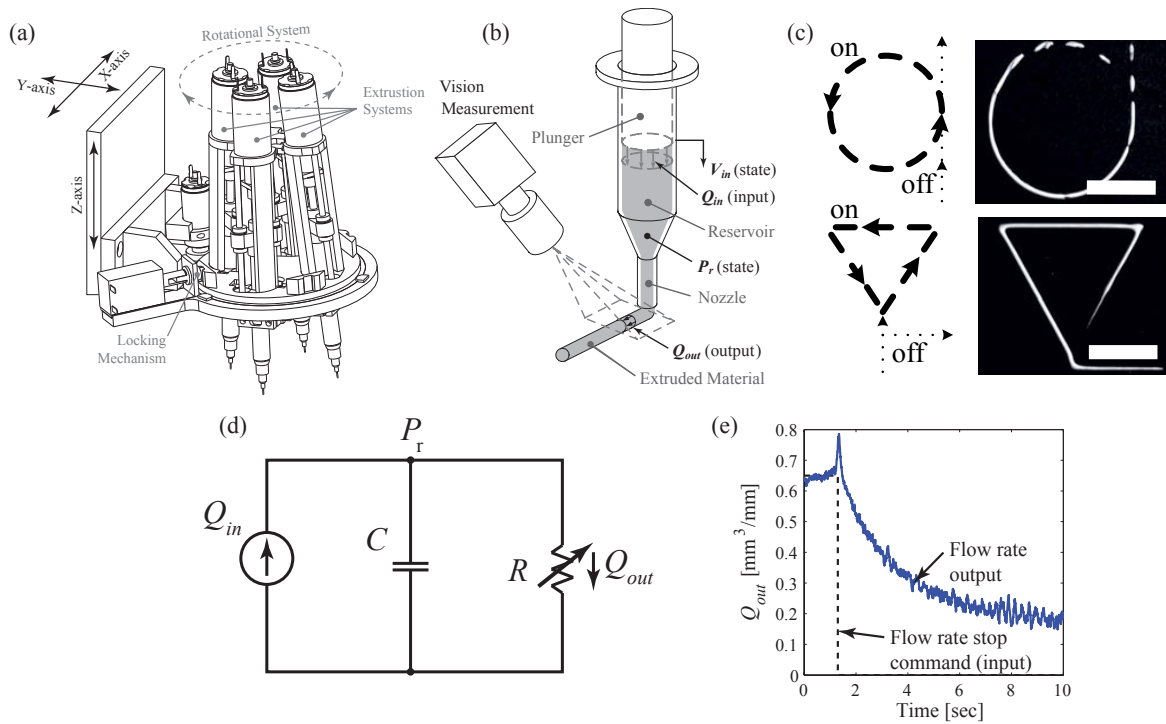


Figure 1: DW printing and challenges in DW flow control. (a) Schematic of DW AM system used to construct two-dimensional hydroxyapatite shapes in [7]. (b) Piston-driven DW extruder head in DW system. Volumetric flow rates (Q_{in} and Q_{out}) are input and output; input volume (V_{in}) and reservoir pressure (P_r) are states. (c) Printing simple shapes with DW demonstrates poor transient flow control [7]. Scale bars are 5 mm. (d) Fluid circuit of DW dynamics, showing capacitive and nonlinear resistive elements. (e) Flow rate output response for input flow rate step from steady state to zero. Output is characteristic of system response with RC time constant. The normalized flow rate over time takes more than 10 seconds to reach zero.

The positive displacement DW system in Figure 1 and used in this paper is the micro robotic deposition system (μ RD). This system has been previously described in [7]. Using a fluid circuit analogy, the dynamics in this DW system can be described as a fluidic capacitance and nonlinear resistance at the reservoir and nozzle walls, respectively (Fig. 1d). Because the plunger in DW acts upon the inlet of the material reservoir, extrusion pressure, P_r , is transmitted throughout the entire material reservoir and is stored within the build material and other compliant elements of the system, acting as a single capacitive element, C . Additionally, the viscoplastic behavior of the build material leads to a nonlinear

resistance to flow, $R(P_r)$, as pressure is applied. Together, these capacitive and resistive elements lead to transient flow rate responses with an observable, pressure dependent RC time constant for typical on or off step inputs (Fig. 1e). Note that normalized volumetric flow rate is used to characterize flow: unit volume per unit length, which provides a measure of cross-sectional area of material delivered. If not stated explicitly, flow rates in this paper refer to the normalized flow rate.

Thus far, modeling of positive displacement DW dynamics in the literature ranges from simplistic, potentially omitting key contributors to the observed phenomena, to highly complex, making their usage in control schemes difficult. Hoelzle et al. [7] modeled DW build materials as pseudoplastic instead of yield-pseudoplastic by assuming small yield stresses. This assumption leads to the formulation in equation (1) and through local linearization about some nominal reservoir volume, V_{r0} , and pressure, P_{r0} , the first order approximation in equations (2) and (3). With this approach, the outflow response to plunger velocity includes a simple delay, λ , to capture the time taken to exceed the material yield stress. While this model proved effective for control system integration, it did not accurately represent flow in some low flow rate transient modes, nor provide a unified method to model both starting and stopping, because $\lambda = 0$ when operating above the build material yield stress, leading to an inability to accurately model stopping conditions.

$$\frac{V_r nD}{\beta_i C} \left(\frac{P_r}{D} \right)^{1-1/n} \dot{Q}_{out} + Q_{out} = A_{cs} \dot{\delta} \quad (1)$$

- V_r = Volume of build material in reservoir
- P_r = Reservoir pressure
- $\dot{\delta}$ = Plunger velocity
- Q_{out} = Control volume outflow
- β_i = Ink bulk modulus
- A_{cs} = Cross-sectional area of plunger
- n = Flow behavior index
- m = Fluid consistency index
- R = Nozzle radius
- L = Nozzle length
- $D_1 = \pi \left(\frac{n}{3n+1} \right) R^{(3n+1)/n}$
- $D_2 = 2mL$

$$\frac{Q_{out}}{\dot{\delta}}(s) = \frac{K}{\tau s + 1} e^{-\lambda s} \quad (2)$$

$$K = A_{cs} \text{ and } \tau = \frac{V_{r0} nD_2}{\beta_i D_1} \left(\frac{P_{r0}}{D_2} \right)^{1-1/n} \quad (3)$$

Conversely, Li et al. [8][9] used a more complex constitutive model for yield-pseudoplastic fluids where apparent viscosity is described by equation (4), a Navier-Stokes equation based framework is used for derivation of build material extrusion response, and build material is assumed compressible with air bubbles present. This work focused on extrusion of aqueous-based ceramic pastes, formulated in terms of extrusion force, F_{ram} , resulting in a first-order nonlinear governing equation.

$$\eta = \begin{cases} \frac{\tau_0}{|\dot{\gamma}|} + m \frac{|\dot{\gamma}|^{n-1}}{\dot{\gamma}_c^{n-1}} & \text{if } |\dot{\gamma}| \geq \dot{\gamma}_c \\ \left[\frac{2\tau_0}{\dot{\gamma}_c} + m(2-n) \right] + \left[\frac{m(n-1)}{\dot{\gamma}_c} - \frac{\tau_0}{\dot{\gamma}_c^2} \right] |\dot{\gamma}| & \text{if } |\dot{\gamma}| < \dot{\gamma}_c \end{cases} \quad (4)$$

- η = Apparent viscosity
- $\dot{\gamma}_c$ = Critical shear rate
- m = Fluid consistency index
- $\dot{\gamma}$ = Shear rate
- τ_0 = Yield stress
- n = Flow behavior index

$$\dot{F}_{ram}(t) = \frac{[F_{ram}(t) - F_f \text{sgn}(u_p) + A_p p_{atm}]^2}{A_p p_c(0) l_0} \left[u_p(t) - P^{-1} \left[\frac{F_{ram}(t) - F_f \text{sgn}(u_p)}{A_p l_p(t)} \right] \right]$$

- A_p = Plunger cross-sectional area
- l_0 = Initial air layer thickness
- p_{atm} = Atmospheric pressure
- F_{ram} = Extrusion force
- l_p = Total length of paste in nozzle
- p_c = Compressible material pressure
- F_f = Friction force between plunger and barrel
- P = Pressure function
- u_p = Plunger velocity

Taken together, this approach resulted in an absolute percent error between experimental and simulated responses of 6.3% in a single extruder system, demonstrating accurate modeling of the transient and steady state dynamics of extrusion of this subset of DW build materials, including the very complex case of air bubbles traveling through the material reservoir and exiting the nozzle. However, the implementation of this model in control architectures faces challenges due to its complexity. Like Hoelzle et al., Li et al. found that for common printing modes, such as when the extrusion force is sufficiently large, the dynamic response is dominated by a first-order response. Additionally, air bubbles can be potentially eliminated from the material reservoir entirely through appropriate system and process design. Thus, the complexity of this model may be unnecessary to capture the majority of the contributors to the observed phenomena of DW printing.

The objective of this work is to synthesize a lumped-parameter gray box model of positive displacement flow of yield-pseudoplastic fluids through a nozzle and to validate the model through extrusion experiments. We seek to model the dominant capacitive elements of DW dynamics and for this model to be directly integrable into nonlinear and linear control schemes. This is accomplished by developing a complex, nonlinear base model which is then linearized into Wiener and linear models. The Wiener model is the middle ground between the nonlinear and linear models, as it provides linear state equations while preserving the nonlinear relationship between state and output. We validate our theoretical work with experimental measurements in the μ RD system, including extrusion of materials that span a diverse set of DW applications - tissue engineering (hydroxyapatite), electronics fabrication (solder paste), and food science (toothpaste) - through varying nozzle sizes. As part of this work, we explore the contribution of build material compliance compared to other compliant elements in the μ RD to the observed dynamics. Through different configurations of the μ RD system, we show that though the bulk system compliance may be reduced, the remaining

compliance due to build material is substantial, preventing satisfactory control of flow and indicating feedback flow control methods are needed.

2 Dynamics of DW Printing

DW operates by leveraging material properties of non-Newtonian fluids. The build material, commonly referred to as ink and typically a suspended ceramic or polymeric slurry or paste, is located in a reservoir upstream of the nozzle. More specifically, DW build materials are yield-pseudoplastic - shear-thinning non-Newtonian fluids with a finite yield stress (Fig. 2a). Nominally, the build material is solid in the reservoir, but by applying sufficient shear stress to the material in the reservoir to overcome the yield stress, the build material begins to flow and is extruded through the nozzle (Fig. 1b). When shear stress is reduced below the yield stress on the build platform, the deposited build material solidifies and holds its shape, facilitating the building of three-dimensional constructs.

Shear stress is typically applied with a pressurized gas (pressure-driven flow) or with a mechanical plunger (positive displacement or plunger-driven flow). Unlike positive displacement flow, pressure-driven flow has the advantage of facilitating reservoir pressure regulation, thereby potentially eliminating the observed dynamic problems. However, unlike pressure-driven flow, positive displacement flow avoids material clogs as a plunger can produce much higher reservoir pressures, expelling material clogs if necessary. Additionally, positive displacement flow allows for more accurate metering of material delivery at steady state due to the finer pressure granularity possible with mechanical driven plungers. With both methods, the removal of shear stresses settles the material into a rigid state to create the final part geometry. Typically, post-processing procedures, such as high temperature sintering, are applied to the solidified part to achieve desired material properties.

We assume an adiabatic process with laminar flow of yield-pseudoplastic fluids. We represent the yield-pseudoplastic build materials with the Herschel-Bulkley constitutive equation

$$\tau = \tau_0 + m\dot{\gamma}^n \quad (5)$$

where for a given shear rate $\dot{\gamma}$, the simple, one-dimensional shear stress, τ , is defined by the yield stress τ_0 , the fluid consistency index or coefficient m , and the flow behavior index or coefficient n [10]. The yield stress prevents flow of the material below a threshold shear stress, a property that is beneficial to 3D printing applications as no material will flow without direct flow rate input. The fluid consistency index is analogous to the apparent viscosity of the fluid, and like power-law modeling of non-Newtonian fluids, the flow behavior index quantifies the shear-thinning of the material, with $n > 1$ corresponding to shear-thickening behavior, $n < 1$ corresponding to shear-thinning behavior, and $n = 1$ being Newtonian. Yield-pseudoplastic fluids will always have $n < 1$. The three Herschel-Bulkley parameters can be measured by standard flow sweep rheometry measurements, which we describe in Section 3.2.

Additionally, we focus our analysis on two domains: compressible flow through the

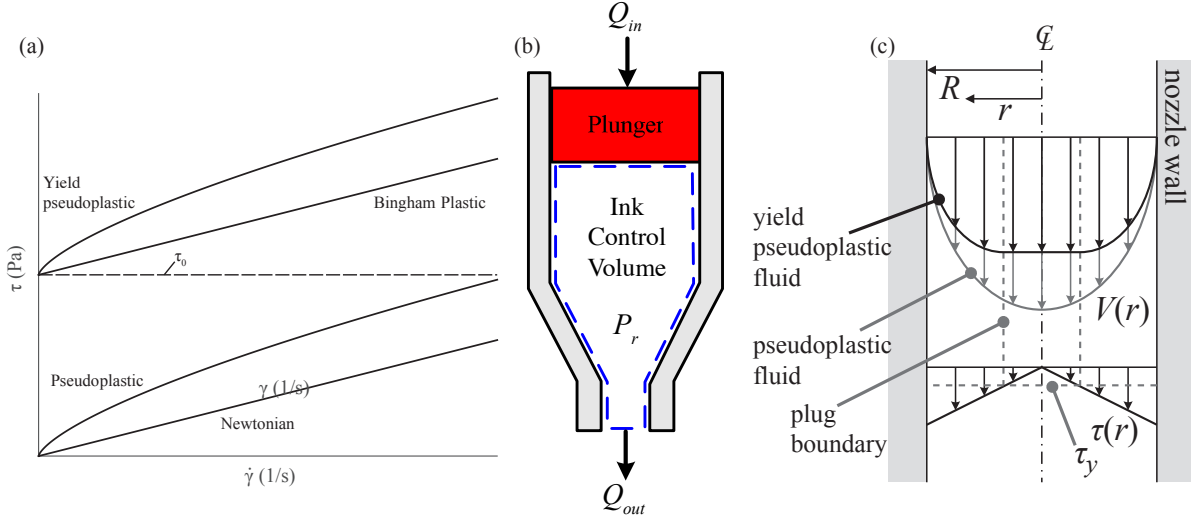


Figure 2: Schematics for model development. (a) Yield-pseudoplastic fluids exhibit both shear thinning and a finite yield stress (τ_0) which must be overcome for flow to begin. Motivated by figure in [10]. (b) Control volume of build material in reservoir. Figure modified from [7]. (c) Velocity and stress distributions of pseudoplastic and yield-pseudoplastic fluid flows in nozzle. Yield-pseudoplastic flow has solid plug at the center surrounded by shear-thinning outer layer at the nozzle wall. Shear stress is maximum at the wall and zero at the center of the plug. Motivated by figure in [10].

reservoir and non-Newtonian flow through the nozzle. For standard DW systems, the reservoir and nozzle domains are an order of magnitude apart in radius and four orders of magnitude in volume, leading to very different governing equations for flow in each domain. For the reservoir domain, consider the control volume in Fig. 2b, where the flow-pressure relationship is governed by

$$\dot{P}_r = \frac{\beta}{V_0 - V_{in}} (Q_{in} - Q_{out}) \quad (6)$$

$$\dot{V}_{in} = Q_{in} \quad (7)$$

- P_r = Reservoir pressure
- V_0 = Initial volume
- Q_{in} = Input volumetric flow rate
- β = Bulk compliance parameter
- V_{in} = Input volume
- Q_{out} = Output volumetric flow rate

which are derived in [7]. Next, the nozzle domain is modeled as yield-pseudoplastic fluid flow through a pipe (Fig. 2c), which is governed by

$$Q_{out} = \begin{cases} \pi R^3 n \left(\frac{\tau_w}{m}\right)^{1/n} (1 - \phi)^{(n+1/n)} \left[\frac{(1-\phi)^2}{3n+1} + \frac{2\phi(1-\phi)}{2n+1} + \frac{\phi^2}{n+1}\right] & \text{for } \phi \leq 1 \\ 0 & \text{for } \phi > 1 \end{cases} \quad (8)$$

- τ_w = Wall shear stress
- m = Fluid consistency index
- τ_0 = Yield stress
- R = Nozzle radius
- n = Flow behavior index
- $\phi = \frac{\tau_0}{\tau_w}$

which is derived in [10]. Consider again the fluid circuit analogy in Fig. 1d. In the reservoir domain, fluidic resistance will have relatively little effect on the dynamics due to the large reservoir radius. However, the large volume of the reservoir introduces a large fluidic capacitance, leading capacitive dynamics to dominate the response in this domain. In the nozzle domain, the nozzle material as well as the small volume minimizes capacitance, but the small radius greatly increases fluidic resistance. Thus, the combined domain system we are seeking to model has both fluidic resistive and capacitive elements, which are apparent in the observed dynamics, which are characteristic of responses with an RC time constant (Fig. 1e).

2.1 Base Nonlinear Model

The base nonlinear model combines the equations for the reservoir and nozzle domains to relate a flow rate at the reservoir inlet to flow rate at the nozzle outlet. This is accomplished with the wall shear stress term, τ_w , which is calculated with

$$\tau_w = \left(\frac{-P_r}{L} \right) \frac{R}{2} \quad (9)$$

which is derived in [10]. Thus, the base nonlinear model integrates equation (6) to find the pressure generated in the material reservoir and then uses equation (8) to find the nozzle output flow rate as a function of this pressure.

To complete the nonlinear model, the system compliance, β , must be found. This term is a bulk parameter element that is a function of the compliance of the build material and the reservoir wall. Note that, generally, additional compliance may be introduced by air trapped in the extruder, but in the μ RD system, air in the reservoir or build material is sufficiently reduced to be assumed negligible. As the exact contribution of the reservoir and build material to the bulk compliance is unknown, β must be determined experimentally for each material. Thus, the base nonlinear model is a gray box model; all variables are geometric measurements or measured by rheometry experiments except for β , which is found for each material from a series of flow rate experiments across a range of nozzle sizes.

2.2 Wiener Model and Linear Model

Both the Wiener and linear models use the same linearization of the nonlinear model for state equations governing pressure and input volume in the reservoir

$$\begin{bmatrix} \frac{d(\hat{V}_{in})}{dt} \\ \frac{d(\hat{P}_r)}{dt} \end{bmatrix} = \begin{bmatrix} 0 & 0 \\ 0 & A_{2,2} \end{bmatrix} \begin{bmatrix} \hat{V}_{in} \\ \hat{P}_r \end{bmatrix} + \begin{bmatrix} 1 \\ \frac{\beta}{V_0 - \bar{V}_{in}} \end{bmatrix} \hat{Q}_{in} \quad (10)$$

where term $A_{2,2}$ is given by

$$A_{2,2} = -\frac{\beta}{V_0 - \bar{V}_{in}} \left. \frac{\partial Q_{out}}{\partial P_r} \right|_{P_r = \bar{P}_r} \quad (11)$$

Linearization is around steady state flow, where input and output flow rates are equal. Choosing steady state flow rate $\bar{Q}_{in} = \bar{Q}_{out} = \pi R^2 v$, the operating points for the system become

$$\begin{cases} \bar{Q}_{in} = \bar{Q}_{out} = \pi R^2 v \\ \bar{V}_{in} = f(\bar{Q}_{out}) \\ \bar{P}_r = g(\bar{Q}_{out}) \end{cases}$$

where v is the nozzle velocity along the printing platform and \bar{V}_{in} and \bar{P}_r are taken from the nonlinear model in steady state flow. The Wiener model maps the linear states to the output flow rate at the nozzle outlet using equation (8). The linear model uses a linearized form of equation (8), equation (12), to map the states to the output flow rate. Derivations of equations 10 and 12 - 15 are presented in the Appendix.

$$Q_{out} = \left. \frac{\partial Q_{out}}{\partial P_r} \right|_{P_r = \bar{P}_r} (\hat{P}_r) + \bar{Q}_{out} \quad (12)$$

Equations (11) and (12) both use the term $\left. \frac{\partial Q_{out}}{\partial P_r} \right|_{P_r = \bar{P}_r}$, which is defined as

$$\left. \frac{\partial Q_{out}}{\partial P_r} \right|_{P_r = \bar{P}_r} = \frac{a\pi}{b} \left(1 - \frac{2L\tau_0}{\bar{P}_r R} \right)^{1/n} \left(\frac{\bar{P}_r R}{2mL} \right)^{1/n} \quad (13)$$

$$a = 48L^3\tau_0^3 n^3 + 24L^2\bar{P}_r R\tau_0^2 n^2 + 6L\bar{P}_r^2 R^2\tau_0 n^2 + 6L\bar{P}_r^2 R^2\tau_0 n + 2\bar{P}_r^3 R^3 n^2 + 3\bar{P}_r^3 R^3 n + \bar{P}_r^3 R^3 \quad (14)$$

$$b = \bar{P}_r^4 (6n^3 + 11n^2 + 6n + 1) \quad (15)$$

Note that both the Wiener and linear models are only valid when $\tau_w > \tau_0$ as flow of the build material only occurs with this relation satisfied. Thus, the pressure term is bounded for all time t such that

$$P_r(t) \geq P_{r,min} = \frac{2L\tau_0}{R} \quad (16)$$

Additionally, in the linear model, eigenvalues are 0 (due to the integrator in equation (7)) and $A_{2,2}$. Thus, the system time constant becomes $\tau = \frac{1}{A_{2,2}}$, where τ is a fluidic RC time constant that characterizes the response of the linear model.

2.3 Model Comparison

The three models take a similar form to relate the reservoir and nozzle domains, with the differences arising in the equations used to describe them. Table (1) summarizes the equations used for the domains in each model.

Table 1: Numbers and linearity of domain equations for each model. Numbers in table are equation numbers.

Model	Reservoir Domain	Mapping between Domains	Nozzle Domain
	States	Wall Shear Stress	Output Flow Rate
Nonlinear	(6), (7) (Nonlinear)	(9)	(8) (Nonlinear)
Wiener	(10) (Linear)	(9)	(8) (Nonlinear)
Linear	(10) (Linear)	(9)	(12) (Linear)

3 Experimental Methods

To validate the models, we compare theoretical output volumetric flow rates to measured output volumetric flow rates of the μ RD system (Sec. 3.2.1). We focus the experiments on transient flow after the input flow rate command steps down from steady state to zero, thus satisfying equation (16) over the time domain tested. In addition to model validation, experimental data provides several variables necessary to complete the models. Namely, the bulk system compliance and steady state flow rates and input volume for the linear models (Sec. 3.2.2, 3.2.3). The parameters for the Herschel-Bulkley constitutive equation are determined by fitting equation (5) to rheometry measurements of shear stress versus shear rate (Sec. 3.2.5). We model and experimentally validate different nozzle sizes for each material to characterize the dynamics across a variety of pressure gradients. This approach makes the models more robust, as bulk compliance terms are found which more accurately represent the material across a wider range of printing use cases and system configurations. The experimental configurations used for model validation are summarized in Table (2).

Table 2: Experimental configurations used for model validations.

Exp. Config.	Nozzle Size	Build Material	Reservoir
1	330 μ m	Hydroxyapatite	Plastic
2	510 μ m		
3	330 μ m	Solder Paste	Plastic
4	510 μ m		
5	330 μ m	Toothpaste	Plastic
6	510 μ m		
7	330 μ m	Toothpaste	Glass
8	510 μ m		

For analysis, we are interested in three areas: (1) accuracy of models to measured flow rates, (2) accuracy of linearized models to nonlinear model, and (3) reduction in system compliance with appropriate configuration changes. We report RMS error between models

and experiment for area 1, RMS of errors between models for area 2, and changes in bulk compliance as a result of a new system configuration for area 3. The system configuration change for analysis area 3 is the use of a non-compliant reservoir made of glass in place of the compliant plastic reservoir typically used in the μ RD. Note that, of the three materials used for experiments, only toothpaste is extruded in this configuration. The suspended particles in hydroxyapatite and solder paste fill the microstructure of the ground glass walls, causing the plunger to seize during deposition.

3.1 Extrusion System

The μ RD consists of a custom extruder assembly attached to an X-Y-Z gantry system (Aerotech ANT 130 EDS145) (Fig. 3). A high-magnification camera (Basler acA1300-30um) is used for machine vision analysis described in Section 3.2.2. The positions and velocities of the extruder subsystems and gantry system are all feedback controlled with high accuracy and do not contribute to the dynamics being modeled.

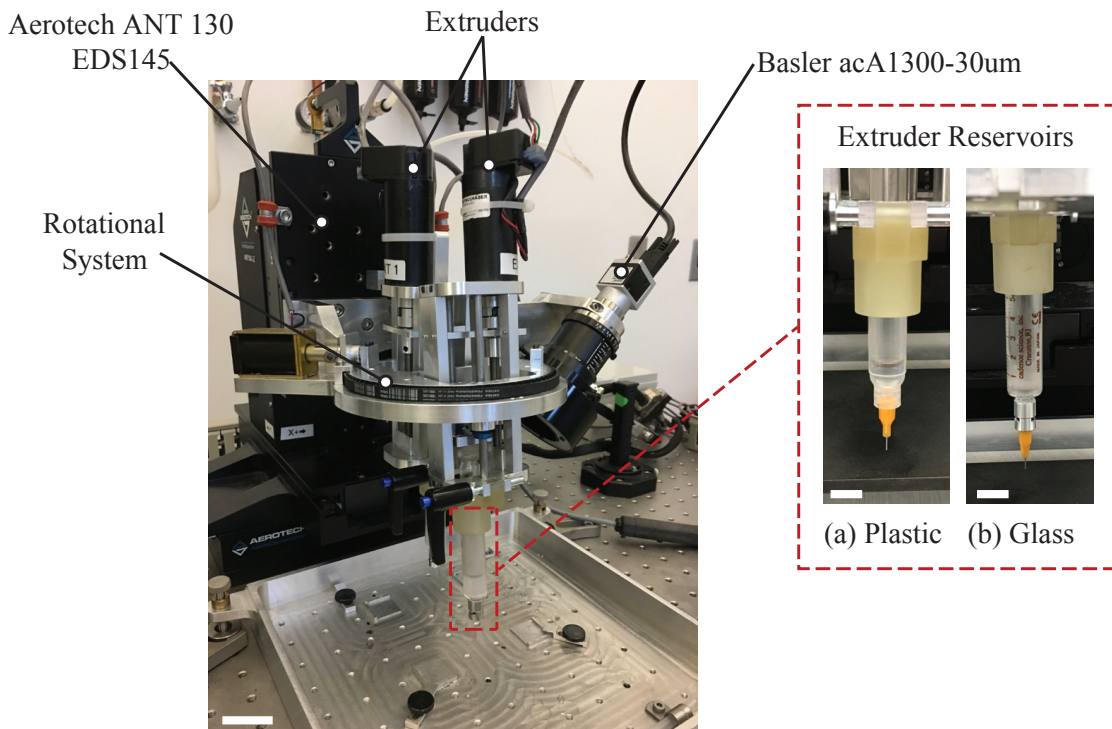


Figure 3: μ RD system consists of Aerotech orthogonal 3-axis gantry system, custom rotational system, and custom extruders. Scale bar is 25mm. Subfigure: Compliant, hard plastic reservoirs and non-compliant, glass reservoirs are used in the μ RD. Scale bars are 10mm.

Each extruder subsystem - consisting of reservoir, plunger, motor with lead screw, and nozzle - is identical. Plastic (Nordson EFD Optimum®) and glass (Cadence Science Perfektum®) syringes are used for reservoirs and blunt-tipped needles (Nordson EFD

7005005 and 7018302 Dispensing Tips) are used for nozzles. The compliant reservoir variant is hard plastic while the non-compliant variant is glass (Subfigure of Fig. 3). We extrude each material through 510 μm and 330 μm deposition nozzles.

The μRD system is controlled with a computer running a custom control program and graphical user interface in Matlab Simulink (ver. R2012b). Quanser Quarc software (ver 2.3.411) is used in conjunction with a Quanser data-acquisition system (QPIDe) for communication between the control computer and μRD hardware. Soloist Motion Composer (ver. 4.05.002) is used to interface with the Aerotech gantry sub-system and Pylon Viewer (ver. 5.0.10.10613) is used to control the camera.

3.2 Methods

3.2.1 Flow Rate Experiments

Pressure is applied to the tested material at the opening of the reservoir by way of a plunger (Fig. 1b). The nozzle velocity, $v = 5\text{mm}$, is the same for both 330 μm and 510 μm nozzle experiments. However, output volumetric flow rate at steady state, $Q_{out} = \pi R^2 v$, will be different for the two nozzle configurations due to differing nozzle radii. Material is extruded in a U-shape (Fig. 4a) to allow flow to reach steady state. The high-magnification camera is attached to the μRD and moves with the extrusion system as printing occurs on the printing platform. The camera is focused at the tip of the nozzle and records the entire deposition process, which is later converted to measurements of flow rate over time using the machine vision analysis described in Section 3.2.2. Two seconds after the second turn in the extrusion path, the input flow command steps down to zero ($Q_{in} = 0$), and the resulting transient output flow rate over time is used for model validation. The deposition procedure is run repeatedly and the resulting flow rate data trials are averaged to reduce noise in the flow rate measurement. For hydroxyapatite and toothpaste, 10 trials were averaged, while for solder paste, 15 trials were averaged.

3.2.2 Machine Vision Analysis

The U-shape deposition process (Fig. 4a) is recorded using a f/8 aperture and 65,000 μs exposure time at 15.4 frames per second. A video processing script (Video_Processing_CF.m, Fig. 4b) takes .avi video files as inputs and outputs volumetric flow rate over time data. The script identifies the first frame of motion using a standard motion detection algorithm (Thresholded Frame Difference [11], Motion.m) and compiles a sequence of frames from this starting point. The first frame of interest, shortly before the input flow rate step down command is sent, is identified. At this frame the user defines the region of interest (ROI) with a rectangular mask (Fig. 4c). The remaining frames are converted to a sequence of binary images based on the defined ROI (inset of Fig. 4c). From these binary images, the width of extruded filament, or rod width (RW), at each point along the trajectory is measured and

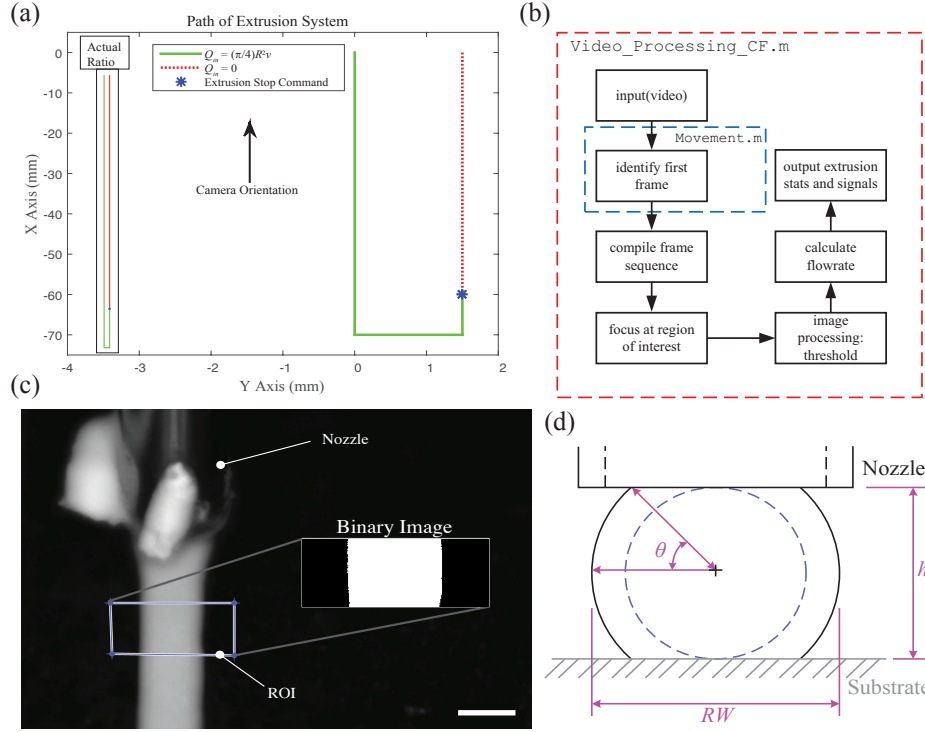


Figure 4: Details of experimental data collection of volumetric flow rate. (a) Material is extruded in U-shape ($Q_{in} = \frac{\pi}{4}R^2v$) before input flow command steps down to zero ($Q_{in} = 0$). (b) Script Video_Processing_CF.m converts video inputs to output volumetric flow rate over time data. (c) As part of video processing algorithm, user defines region of interest (ROI). Scale bar is $250\mu\text{m}$. Inset: Frames of interest are converted to sequence of binary images based on defined ROI. (d) Assumed cross-section of extruded build material for volumetric flow rate calculations.

used to calculate volumetric flow rate with

$$Q_{out} = \begin{cases} \frac{\pi}{4}RW^2v & \text{for } 0 \leq RW \leq h \\ \left(\frac{1}{2}\theta RW^2 + \frac{1}{2}h^2 \frac{1}{\tan \theta} \right) v_x & \text{for } RW > h \end{cases} \quad (17)$$

where h is the standoff height between the nozzle and the substrate, $\theta = \sin^{-1}\left(\frac{h}{RW}\right)$, and v is the forward velocity of the nozzle. Equation (17) assumes the extruded fluid is a rod with cross-section shown in Figure 4d, an assumption supported by [6].

3.2.3 β Selection

The bulk compliance term, β , is determined by maximizing the normalized mean square error, E_{NMS} , between the nonlinear model volumetric flow rate data, $(Q_{out})_{nm}$, and the experimental volumetric flow rate data, $(Q_{out})_{exp}$. E_{NMS} , equation (18), ranges from zero to unity, with unity indicating a perfect match between compared data sets. For a

given material, each tested β value is used to run a simulation of the nonlinear model in both $330\mu\text{m}$ and $510\mu\text{m}$ configurations. The resulting errors are averaged to find a single error term as a function of β . The procedure is repeated with finer granularity bounds on β until the β term that produces the averaged E_{NMS} closest to unity with 3 significant figures is found. The pseudo-code in Algorithm (1) describes the β selection procedure.

Algorithm 1: β Selection

```

1 function findBeta (( $Q_{out}$ )exp,1, ( $Q_{out}$ )exp,2);
   Input  :  $330\mu\text{m}$  ( $Q_{out}$ )exp data: ( $Q_{out}$ )exp,1,  $510\mu\text{m}$  ( $Q_{out}$ )exp data: ( $Q_{out}$ )exp,2
   Output: Chosen  $\beta$  for given material data
2 cont = 1;
3 while cont = 1 do
4     define: a ( $\beta$  lower bound);
5     define: b ( $\beta$  lower bound);
6     define: step ( $\beta$  step size);
7      $\beta_{test}(i) = a : step : b$ ;
8     for  $i = 1 : \text{length}(\beta_{test})$  do
9         calculate:  $330\mu\text{m}$  ( $Q_{out}$ )nm using  $\beta_{test}(i)$ ;
10        calculate:  $510\mu\text{m}$  ( $Q_{out}$ )nm using  $\beta_{test}(i)$ ;
11        calculate:  $E_{NMS,1}$  with  $330\mu\text{m}$  ( $Q_{out}$ )nm and ( $Q_{out}$ )exp,1;
12        calculate:  $E_{NMS,2}$  with  $510\mu\text{m}$  ( $Q_{out}$ )nm and ( $Q_{out}$ )exp,2;
13         $E_{NMS}(i) = \text{mean}(E_{NMS,1}, E_{NMS,2})$ ;
14    end
15    display to user:  $\max(E_{NMS}(i))$ ;
16    display to user:  $\beta$  corresponding to  $\max(E_{NMS}(i))$ ;
17    define: cont
18 end

```

For a given nonlinear model and experimental volumetric flow rate data sets, the normalized mean square error is found with

$$E_{NMS}(t, k) = 1 - \frac{\|(Q_{out})_{exp} - (Q_{out})_{nm}\|^2}{\|(Q_{out})_{exp} - \text{mean}((Q_{out})_{exp})\|^2} \quad (18)$$

where $\|\cdot\|$ denotes the Euclidean norm, t is the time index, and k is the configuration index corresponding to $330\mu\text{m}$ or $510\mu\text{m}$ data sets. The two-step averaging described in Algorithm 1 averages each configuration data set over time (steps 11 and 12) and then averages the two configurations together (step 13). With this approach, a single β is found for each material and used for all three models.

3.2.4 Model Errors

To calculate the deviation of models from experimental data the percent error is found using

$$\%Error(t) = \left| \frac{(Q_{out})_{exp} - (Q_{out})_{model}}{(Q_{out})_{exp}} \right| * 100 \quad (19)$$

where $(Q_{out})_{exp}$ and $(Q_{out})_{model}$ correspond to the experimental and model volumetric flow rate data for a chosen material, nozzle, and model type. Equation (19) results in an array of percent error at each time step; this array is averaged over time to produce a single percent error term for the given experimental configuration.

3.2.5 Rheometry

For each material, flow sweeps of shear stress, τ , versus shear rate, $\dot{\gamma}$, are measured. A Discovery HR-2 (TA Instruments) rheometer is used with 40mm diameter parallel plate geometry. Shear stress measurements are taken for 6.5×10^{-2} to 6.5×10^2 1/s, the range of possible shear rates in the μ RD system, in logarithmic steps with resolution 10 pts/decade at steady state temperature 25°C. For hydroxyapatite, the shear rate resolution was 5 pts/decade to prevent evaporation during testing. Steady state sensing is used; a measurement for a given shear rate is recorded only if 3 consecutive measurements taken within 120 seconds do not exceed 5% deviation. Only steady state measurements points are presented in the results. For each material, 5 flow sweeps are captured and averaged together to produce the final flow sweep for the material. This flow sweep is fit to the Herschel-Bulkley model (equation (5)) to determine the three parameters of the constitutive equation for the given material.

3.3 Materials

To represent a broad range of DW printing applications, we chose a set of diverse yield-pseudoplastic materials: solder paste (Nordson RMA-D200 T2, Sn63/Pb37, P/N: 7020311) used in industrial electronics, toothpaste (Colgate Total Whitening) used in food science, and hydroxyapatite used in tissue engineering. Hydroxyapatite was formulated using the procedures outlined in [12][13] with a concentration of 50% HA powder.

4 Results

For the three extruded materials, rheometry flow sweeps are presented in Figure 5 and Herschel-Bulkley parameters are presented in Table 3. The fit of the rheometry data to equation (5) was excellent, as each material had an R^2 value of >0.99 . Solder paste was found to have the highest yield stress, nearly twice that of the toothpaste, which had the lowest. Hydroxyapatite was found to be the most viscous, with a fluid consistency index two orders of magnitude higher than solder paste and toothpaste. Additionally, hydroxyapatite

had a much lower flow behavior index than solder paste and toothpaste, indicating greater shear-thinning behavior.

Table 3: Herschel-Bulkley parameters for extruded materials.

Materials	τ_0 [Pa]	m [Pa·s ^{<i>n</i>}]	n	R^2
Hydroxyapatite	190.69	1370.93	0.39	>0.99
Solder Paste	299.20	42.03	0.78	>0.99
Toothpaste	144.43	76.17	0.70	>0.99

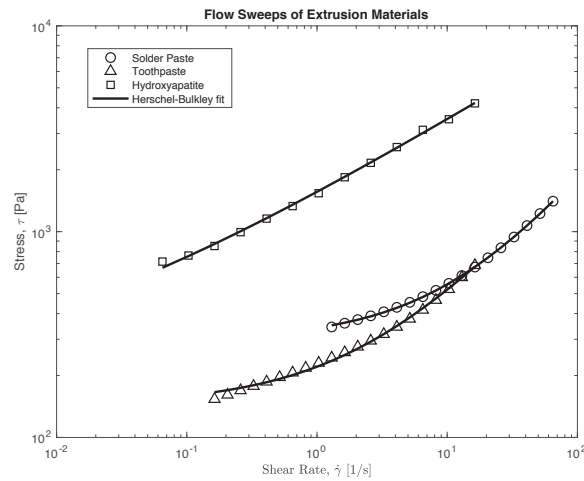
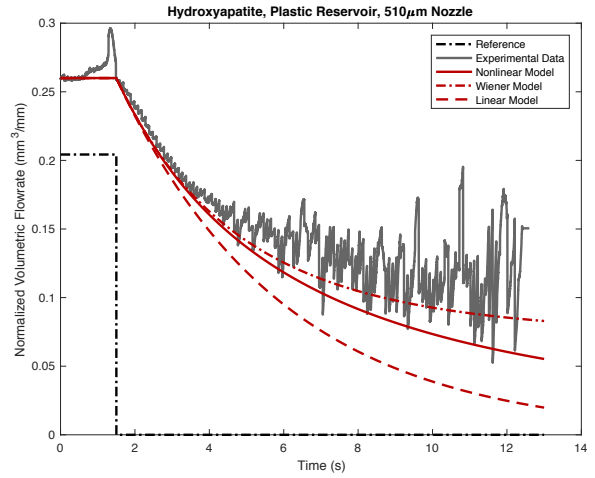
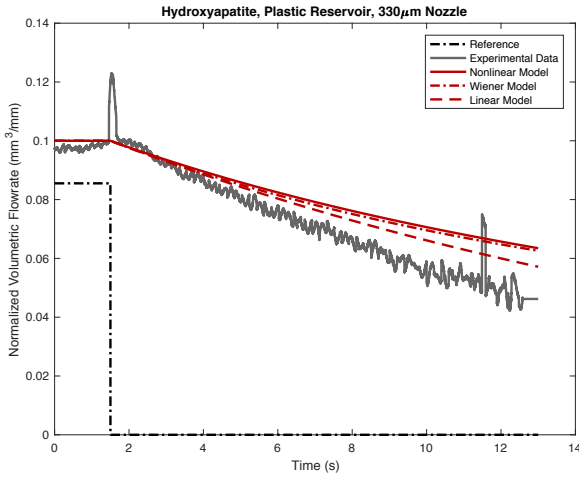


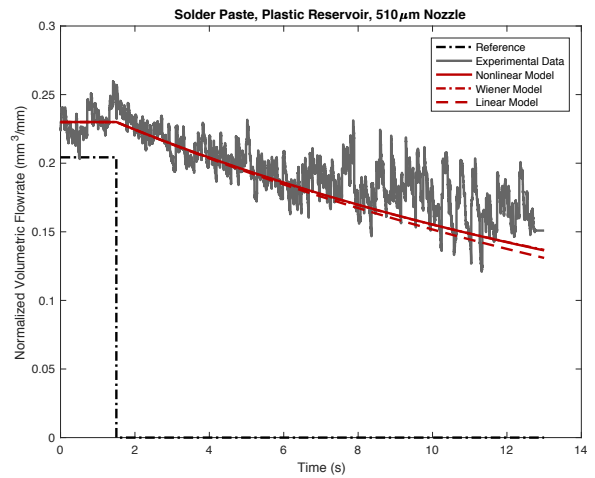
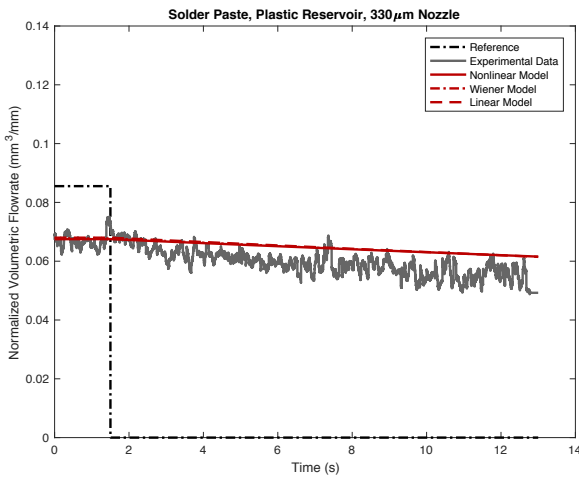
Figure 5: Rheology flow sweeps for extruded materials.

Output volumetric flow rate over time for each experimental configuration compared to the respective model simulations for the configuration are presented in Figures 6 - 9.



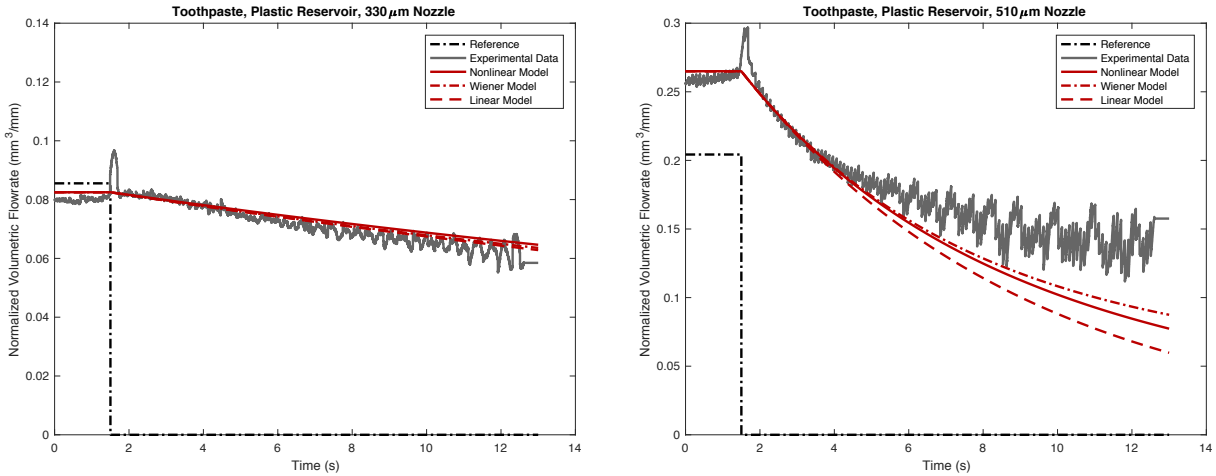
(a) 330 μm nozzle - Experimental configuration 1 (b) 510 μm nozzle - Experimental configuration 2

Figure 6: Output volumetric flow rates over time for hydroxyapatite.



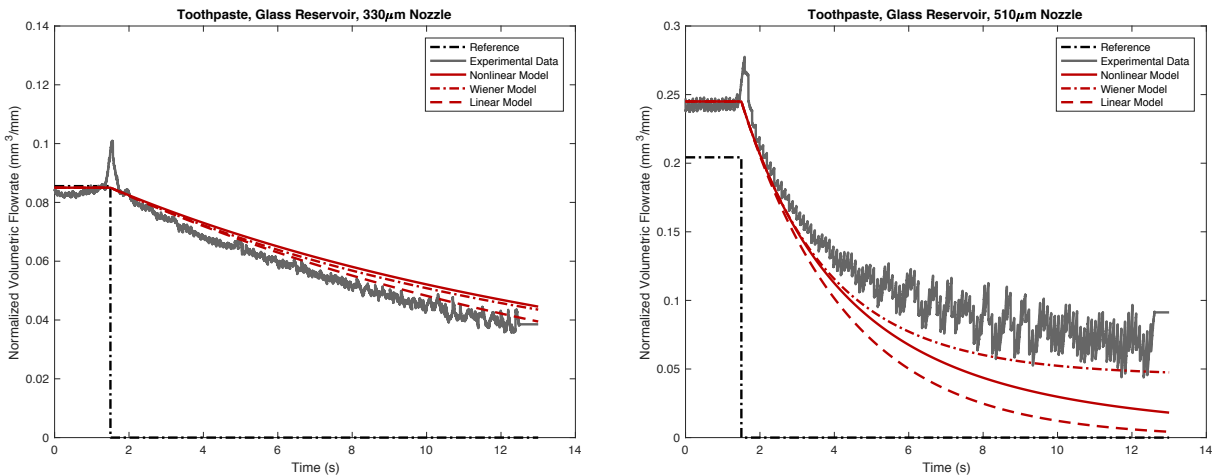
(a) 330 μm nozzle - Experimental configuration 3 (b) 510 μm nozzle - Experimental configuration 4

Figure 7: Output volumetric flow rates over time for solder paste.



(a) $330\mu m$ nozzle - Experimental configuration 5 (b) $510\mu m$ nozzle - Experimental configuration 6

Figure 8: Output volumetric flow rates over time for toothpaste with plastic reservoir.



(a) $330\mu m$ nozzle - Experimental configuration 7 (b) $510\mu m$ nozzle - Experimental configuration 8

Figure 9: Output volumetric flow rates over time for toothpaste with glass reservoir.

As discussed in Section 2.2, eigenvalues of the linear model are 0 and $A_{2,2}$ and the decay of the system is characterized by $\tau = \frac{1}{A_{2,2}}$, where τ is the fluidic RC time constant. Thus, with changes in the reservoir wall from compliant plastic to non-compliant glass, we can study changes in bulk system compliance and time constant of the linear model transient response. The output volumetric flow rates of toothpaste printed with different reservoirs are presented in Figure 10, where relevant changes in time constant are highlighted.

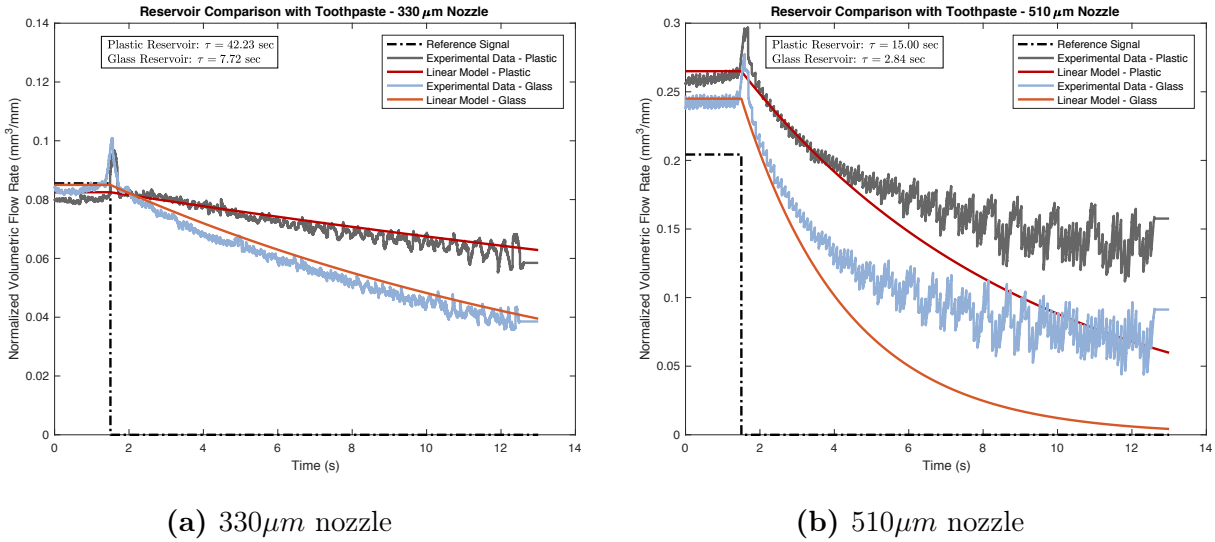


Figure 10: Comparison of output volumetric flow rates over time for toothpaste with compliant and non-compliant reservoir.

Percent errors of models to experiment are collected in Table 4; the chosen β value for each material is included in this table. The percent differences of linearized models to the nonlinear model are collected in Table ??.

Table 4: Percent errors of models to experiment. Units are percent. HA = Hydroxyapatite, SP = Solder Paste, TP = Toothpaste.

Material	β [Pa]	%Error					
		330 μ m nozzle			510 μ m nozzle		
		Nonlinear	Wiener	Linear	Nonlinear	Wiener	Linear
HA	1.37×10^8	14.23	13.13	9.95	23.05	15.21	37.74
SP	6.41×10^6	8.92	9.23	9.20	7.45	7.46	8.30
TP (Plastic)	2.04×10^7	4.02	3.35	3.08	16.06	13.88	21.13
TP (Glass)	5.67×10^7	10.17	8.41	5.36	35.64	20.24	50.01

5 Discussion and Conclusions

We see reasonable agreement between models and experimental data, with good to very good agreement for specific configurations. Looking at configurations across materials, we see that solder paste and toothpaste were modeled better than hydroxyapatite, with solder paste being the best modeled material over both nozzle types. For all materials, we found lower percent error for configurations using 330 μ m nozzles, though this is expected given the noisier experimental data recorded with 510 μ m nozzles. Looking at Figures 6 - 9, we see that modeling for 510 μ m data was more accurate earlier in time, which is partly explained by the difficulty in accurately recording low flow rates. Near the end of a given

flow rate experiment with a $510\mu\text{m}$ nozzle, the material has more difficulty attaching to the printing platform due to lower reservoir pressure, which leads to both increased noise and an offset in the recorded flow rate for the tail end of the dynamic response. We also saw the worst overall percent errors in the modeling of $510\mu\text{m}$ configurations, with the worst 3 configurations having percent errors ranging from 35 - 50%.

Looking at the percent errors of models in more detail, the Wiener model was best, followed by the nonlinear model and the linear model. More specifically, the Wiener model was the best model for 3 configurations, the second best for 4 configurations, and the worst for 1 configuration. The linear model was also the best for 3 configurations, but, conversely, the worst for 4 configurations. The nonlinear model was the second best model overall with 2, 3, and 3 configurations where it was the best, second best, and worst model, respectively. This implies that simplified linear modeling of DW dynamics is often more accurate, and importantly for future applications, moving to a linearized model like the Wiener model for a control scheme implementation will not incur a high cost in terms of modeling accuracy loss. Though we found the linear model to be the worst approximation of the experimental data, we may still consider it for future control implementation due to its ease of implementation and acceptable percent errors ($<10\%$) for the majority of experimental configurations (5 of 8). Lastly, note that we observed poor agreement of all models to the measured data at the boundary of steady state and transient flows, but that this is expected. The spike observed in the measurements is an artifact of the μRD , as the system is programmed to decelerate the stage into and accelerate the stage out of plunger velocity changes.

The machine vision algorithm introduces noise across the entire range of measured flow as a result of the image conversion used for flow rate quantification; small experimental setup deviations further contribute to this issue. In simplest terms, the binary image conversion that is conducted as part of the machine vision procedure introduces errors inside and outside of the actual flow stream; pixels outside the stream can register as white indicating material deposited and pixels inside the stream can register as black, indicating no material or holes in the flow. As shown in Figure 4c, for materials with a high contrast, such as hydroxyapatite and toothpaste, this issue is less problematic. However, for solder paste, the lack of contrast to the dark printing platform and the diffuse particle suspension composition of the build material noticeably increases noise in the measurement.

We examined the contribution of reservoir and build material to bulk system compliance. Reducing reservoir compliance clearly reduced system compliance as we see a percent change of β for toothpaste of 177%, a nearly two-fold reduction. However, the compliance from build material alone still produces dynamics that are problematic for accurate metering of flow. Furthermore, there is no way to eliminate material compliance as this property is intrinsic to any fluid. Thus, all positive displacement DW systems face this problem and further engineering effort is required to improve performance.

In future work, we plan to address these dynamics through the use of feedback control of reservoir pressure using the linearized model presented in this work. Zhao et al. [14] showed good tracking performance of extrusion force using a feedback control system. More commonly, feedforward methods are used [15][16], though system nonlinearities and modeling errors can limit the effectiveness of these techniques or make them difficult to implement.

As real-time flow rate sensors for the μL volumes that are delivered by DW systems of this type are not yet realized, we feel the most direct way to implement feedback controllers for material delivery is to control the reservoir pressure. We plan to explore these challenges in controller design in simulation and then hardware implementation in future work. The current work provides the platform for understanding these problems and the tools to address them.

6 Acknowledgments

Support for this research was provided in part by NSF CAREER Award CMMI 1708819 and NSF GRFP Award DGE-1343012. The authors wish to acknowledge Professor Yael Vodovotz and Drs. Sravanti Paluri and John Frelka for their training, guidance, and support during rheometry testing, and for the usage of rheometers. We acknowledge Ashley Allison Armstrong and Professor Amy J. Wagoner Johnson for providing hydroxyapatite build material for this work. We acknowledge Stephen Bedard for early work on the nonlinear modeling presented here. We acknowledge Kevin Wolf for machining custom reservoir holders.

7 Appendix - Derivation of Linear State and Output Equations

The linearized state space model for the reservoir domain takes the form

$$\begin{bmatrix} \frac{d(\hat{V}_{in})}{dt} \\ \frac{d(\hat{P}_r)}{dt} \end{bmatrix} = \begin{bmatrix} A_{1,1} & A_{1,2} \\ A_{2,1} & A_{2,2} \end{bmatrix} \begin{bmatrix} \hat{V}_{in} \\ \hat{P}_r \end{bmatrix} + \begin{bmatrix} B_1 \\ B_2 \end{bmatrix} \hat{Q}_{in}$$

By inspection, linearization of equation (7) using $V_{in} = \hat{V}_{in} + \bar{V}_{in}$ yields

$$\begin{cases} A_{1,1} = 0 \\ A_{1,2} = 0 \\ B_1 = 1 \end{cases}$$

Linearizing equation (6) using

$$\begin{cases} P_r = \hat{P}_r + \bar{P}_r \\ Q_{in} = \hat{Q}_{in} + \bar{Q}_{in} \\ Q_{out} = \hat{Q}_{out} + \bar{Q}_{out} \end{cases}$$

yields

$$\begin{aligned} \frac{d(\hat{P}_r)}{dt} &\approx \left. \frac{\partial \dot{P}_r}{\partial V_{in}} \right|_{\bar{P}_r, \bar{V}_{in}, \bar{Q}_{in}, \bar{Q}_{out}} (V_{in} - \bar{V}_{in}) + \left. \frac{\partial \dot{P}_r}{\partial P_r} \right|_{\bar{P}_r, \bar{V}_{in}, \bar{Q}_{in}, \bar{Q}_{out}} (P_r - \bar{P}_r) + \\ &\quad \left. \frac{\partial \dot{P}_r}{\partial Q_{in}} \right|_{\bar{P}_r, \bar{V}_{in}, \bar{Q}_{in}, \bar{Q}_{out}} (Q_{in} - \bar{Q}_{in}) + \left. \frac{\partial \dot{P}_r}{\partial Q_{out}} \right|_{\bar{P}_r, \bar{V}_{in}, \bar{Q}_{in}, \bar{Q}_{out}} (Q_{out} - \bar{Q}_{out}) \end{aligned}$$

which when evaluated yields the following parameters

$$\begin{cases} A_{2,1} = 0 \\ A_{2,2} = -\frac{\beta}{V_0 - \bar{V}_{in}} \frac{\partial Q_{out}}{\partial P_r} \Big|_{P_r = \bar{P}_r} \\ B_2 = \frac{\beta}{V_0 - \bar{V}_{in}} \end{cases}$$

Term $A_{2,2}$ can be further evaluated to find

$$A_{2,2} = -\frac{\beta}{V_0 - \bar{V}_{in}} \frac{a\pi}{b} \left(1 - \frac{2L\tau_0}{\bar{P}_r R}\right)^{1/n} \left(\frac{\bar{P}_r R}{2mL}\right)^{1/n}$$

$$\begin{aligned} a &= 48L^3\tau_0^3n^3 + 24L^2\bar{P}_r R\tau_0^2n^2 + 6L\bar{P}_r^2 R^2\tau_0n^2 + 6L\bar{P}_r^2 R^2\tau_0n + 2\bar{P}_r^3 R^3n^2 + 3\bar{P}_r^3 R^3n + \bar{P}_r^3 R^3 \\ b &= \bar{P}_r^4 (6n^3 + 11n^2 + 6n + 1) \end{aligned}$$

Using a similar procedure, the linearized output equation used in the full linearized model is found. Defining the linearization relations and linearizing equation (8) results in equation (20), which may be solved to find equation (21), which is readily solved using the preceding solution.

$$\begin{cases} P_r = \hat{P}_r + \bar{P}_r \\ Q_{out} = \hat{Q}_{out} + \bar{Q}_{out} \\ \hat{Q}_{out} = \frac{\partial Q_{out}}{\partial P_r} \Big|_{P_r = \bar{P}_r} (P_r - \bar{P}_r) \end{cases} \quad (20)$$

$$Q_{out} = \frac{\partial Q_{out}}{\partial P_r} \Big|_{P_r = \bar{P}_r} (\hat{P}_r) + \bar{Q}_{out} \quad (21)$$

References

- [1] I. Gibson, D. Rosen, and B. Stucker, *Additive Manufacturing Technologies: 3D Printing, Rapid Prototyping, and Direct Digital Manufacturing*, 2nd ed. New York: Springer, 2015.
- [2] D. Gu, *Laser Additive Manufacturing of High-Performance Materials*, 1st ed. New York: Springer, 2015.
- [3] A. Deliormanli and M. Rahaman, “Direct-write assembly of silicate and borate bioactive glass scaffolds for bone repair,” *Journal of the European Ceramic Society*, vol. 32, no. 14, pp. 3637–3646, 2012.
- [4] S. J. Hollister, “Porous scaffold design for tissue engineering,” *Nature Materials*, vol. 4, pp. 518–524, 2005.
- [5] P. Bajaj, R. M. Schweller, A. Khademhosseini, J. L. West, and R. Bashir, “3D Biofabrication Strategies for Tissue Engineering and Regenerative Medicine,” *Annual Review of Biomedical Engineering*, vol. 16, pp. 247–76, 2014.
- [6] J. Cesarano III, R. Segalman, and P. Calvert, “Robocasting provides moldless fabrication from slurry deposition,” *Ceramic Industry*, vol. 148, no. 4, pp. 94–102, 1998.
- [7] D. J. Hoelzle, A. G. Alleyne, and A. J. Wagoner Johnson, “Iterative Learning Control for Robotic Deposition Using Machine Vision,” in *American Control Conference*, 2008, pp. 4541–4547.
- [8] M. Li, L. Tang, R. G. Landers, and M. C. Leu, “Extrusion Process Modeling for Aqueous-Based Ceramic Pastes - Part 1: Constitutive Model,” *Journal of Manufacturing Science and Engineering*, vol. 135, no. October 2013, pp. 051 008–1 – 051 008–7, 2013.
- [9] —, “Extrusion Process Modeling for Aqueous-Based Ceramic Pastes - Part 2 : Experimental Verification,” *Journal of Manufacturing Science and Engineering*, vol. 135, no. October 2013, pp. 051 009–1 – 051 009–7, 2013.
- [10] R. Chhabra and J. Richardson, *Non-Newtonian Flow and Applied Rheology: Engineering Applications Second Edition*, 2nd ed. Oxford: Elsevier Ltd, 2008.
- [11] E. Martinez-Martin and A. P. del Pobil, *Robust Motion Detection in Real-Life Scenarios*, 1st ed. New York: Springer, 2012.
- [12] S. Michna, W. Wu, and J. A. Lewis, “Concentrated hydroxyapatite inks for direct-write assembly of 3-D periodic scaffolds,” *Biomaterials*, vol. 26, no. 28, pp. 5632–5639, 2005.
- [13] D. J. Hoelzle, “Flexible Adaptation of Iterative Learning Control with Applications to Synthetic Bone Graft Manufacturing,” Dissertation, University of Illinois at Urbana-Champaign, 2011.

- [14] X. Zhao, R. G. Landers, and M. C. Leu, “Adaptive Extrusion Force Control of Freeze-Form Extrusion Fabrication Processes,” *Journal of Manufacturing Science and Engineering*, vol. 132, no. 6, pp. 064504–1 – 064504–9, 2010.
- [15] D. J. Hoelzle, “Reliability Guidelines and Flowrate Modulation for a Micro Robotic Deposition System,” Masters Thesis, University of Illinois at Urbana-Champaign, 2007.
- [16] W. Han and M. A. Jafari, “Coordination Control of Positioning and Deposition in Layered Manufacturing,” *IEEE Transactions on Industrial Electronics*, vol. 54, no. 1, pp. 651–659, 2007.